A New Hybrid Concentrated-Winding Concept with Improved Power Factor for Permanent Magnet Vernier Machine

Shuangchun Xie, Shun Cai, *Member*, *IEEE*, Yuefei Zuo, *Member*, *IEEE*, Libing Cao, *Member*, *IEEE*, Jingwei Zhu, An Li, Yuming Yan, and Christopher H.T. Lee, *Senior Member*, *IEEE*

***Abstract*—This paper investigates a high power-factor permanent magnet vernier machine (PMVM) equipped with low-coupling hybrid concentrated-winding (CW). The proposed hybrid-CW, carrying both star- and delta-winding sets, exhibits a good filtering property to both sub- and super-order harmonics. Through the meticulous design of the short coil pitch, the ratio of inductance to magnet flux linkage is decreased, leading to a great improvement in power factor. The proposed low-coupling winding design contributes to further power factor improvement by reducing the inductance while retaining the magnet flux linkage. It is revealed that the mutual coupling between different coils of single phase and that between different windings of three phases are suppressed significantly in the hybrid-CW, thus leading to high power factor and potentially high fault tolerance. Finite element results show that the proposed hybrid-CW PMVM exhibits a significantly improved power factor up to 0.96 from 0.83 and 0.75, as compared with two counterpart PMVMs with open-slot and split-tooth structures, respectively. Benefiting from the magnetic gearing effect, the proposed PMVM has a promising active torque density of 40 Nm/L. Taking end-winding volume into consideration, the proposed PMVM exhibits an actual torque density of 21.98 Nm/L, which is 22.52% and 52.43% higher than the investigated open-slot and split-tooth counterpart PMVMs. Finally, a prototype is fabricated and tested to validate the high-power-factor and high-torque-density features of the proposed hybrid-CW PMVM.**

***Index Terms*—Permanent magnet, vernier machine, concentrated-winding, low-coupling, power factor.**

I. Introduction

In the past few decades, the demand for direct-drive machines has been increasing in various applications, such as electric vehicles, industrial robots, domestic appliances, and wind power generation [1]-[5]. Even the popular permanent magnet synchronous machine can provide excellent performances in various aspects, it can hardly fulfil the low-speed high-torque requirements without installation of reduction gear. Based on field modulation mechanism, the permanent magnet vernier machine (PMVM) exhibits high output torque with the modulation effect of stator teeth [6]-[8]. Thus, PMVMs are acknowledged as one of the promising candidates for direct-drive applications.

In spite of high torque production capability, PMVMs are subject to inherently low power factors, resulting in bulky size and high cost of the inverter. Numerous researches have been conducted to improve the power factor. Novel rotor topologies with different PM arrangements have been investigated to improve the power factor by enhancing the magnetic loading, such as consequent pole [9], Halbach array [10], spoke-type [11], and U-type PMs [12]. Among these various topologies, the spoke-type PMVMs exhibit the most promising performance by flux focusing effect, while the field modulation is weakened by the flux barrier effect. To overcome the flux barrier issue and further enhance the power factor, the spoke-type with flux bridge and double-stator structures have been proposed to improve the flux path for low pole-pair working magnetic field [13]-[16]. Although the foregoing topologies can effectively improve the power factor, the increased PM cost and manufacturing difficulty hinder their practical applications.

Other than new rotor topologies, reducing armature flux linkage harmonics has been identified as alternative solutions for achieving high power factors. In [17] and [18], it was illustrated that the PMVMs with two-slot pitch winding, as one of the forms of overlapping distributed winding (DW), exhibit higher power factors than those with non-overlapping concentrated winding (CW), due to the elimination of abundant armature magnetic field harmonics. Meanwhile, the output torque is deteriorated since the armature flux linkage has crucial but reverse effects on output torque and power factor. PMVMs are generally susceptible to long end-winding problem with overlapping DW arrangement. To achieve a high pole ratio and high output torque, a stator with a large slot number and a small pole number is preferred in PMVMs. As compared with CW, DW exhibits a better filtering property to armature field harmonics, leading to an improved power factor. Therefore, DW with long end-winding is usually employed in PMVMs. To shorten the end-winding length, toroidal windings and CWs have been applied to PMVMs [19]-[21]. However, the single-rotor PMVMs with toroidal windings suffer from low winding factor and deteriorated output torque capability. Meanwhile, CWs are usually equipped with split-tooth stator structure to achieve high winding factor and high pole ratio. This winding structure is subject to abundant armature field harmonics, low slot area utilization, and more severe flux leakage, resulting in impaired power factor and output torque production.

In this paper, the hybrid-CW incorporating both star- and delta-winding sets is introduced to PMVMs to address the low power factor and long end-winding problems. It has been

proven that hybrid star-delta winding exhibits higher fundamental winding factor and reduced MMF harmonic contents [22]. Therefore, the hybrid star-delta winding has been employed in various machine types, with emphasis on improving output torque and efficiency [23]-[26]. Besides, the hybrid star-delta winding has attracted increasing attentions in PM machines equipped with CWs. The abundant MMF harmonics of CWs can be eliminated by meticulously designed hybrid star-delta winding, contributing to lower rotor eddy current losses, lower torque ripple, and higher machine saliency [27]. Furthermore, the hybrid star-delta winding is employed to achieve a wider constant power speed range (CSPR), attributed to the high voltage utilization of the internal delta winding [28]. It should also be noted that the hybrid star-delta winding exhibits superiority when a fault occurs. Specifically, the star-delta winding can output twice output torque as the conventional star winding when one phase is missing [29]. More importantly, the delta winding can provide a short-circuit current path for the zero-sequence current when short-circuit fault occurs, thereby restricting the fault current [30].

Even though the hybrid-CW has been widely applied in conventional PM machines to achieve higher output torque and higher efficiency, its application in PMVMs is rarely investigated. In this paper, a hybrid-CW PMVM is investigated, with focus on various inductance components and power factor improvement. The analysis of armature magnetomotive force (MMF) distribution shows that the hybrid-CW exhibits a superior filtering property to both sub- and super-order MMF harmonics, which is beneficial for obtaining high power factor. Through the meticulous design of short coil pitch, the inductance is reduced more significantly than the magnet flux linkage, resulting in a substantially improved power factor. Theoretical analysis verifies that the proposed low-coupling design leads to further improvement in power factor without impairing the magnet flux linkage. The low-coupling design has twofold essences, namely the coupling between different coils of one phase and the mutual coupling among three phases are reduced to a large extent. As a result, the inductance is further reduced and the power factor is improved, with retained magnet flux linkage and torque production capability. Although the pitch factor is lower due to the adopted short coil pitch, the actual torque density of the proposed PMVM is enhanced with the reduced end-winding length and more compact structure. The electromagnetic performances of the proposed hybrid-CW PMVM are compared with two conventional PMVMs with open-slot and split-tooth structures, termed as Motor 1 and Motor 2, respectively. Finally, a prototype is manufactured to verify the proposed concepts.

II. The Proposed Hybrid Concentrated Winding

A. Machine Topology and Working Principle

Fig. 1 (a) shows the cross section of the proposed hybrid-CW PMVM with 18-stator slot, 5-armature pole pair, and 13-rotor pole pair. As demonstrated in Fig. 1 (b), the spoke-type PM arrangement is adopted to enhance the magnetic field by flux focusing effect. The flux bridge is utilized to mitigate the associated flux barrier problem, improve field modulation, and increase output torque [13], [14]. The proposed hybrid-CW utilizes tooth-wound winding, which consists of two winding

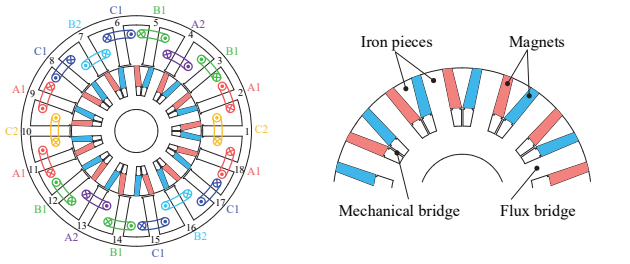

Fig. 1. Proposed hybrid-CW PMVM. (a) Topology. (b) Rotor Structure.

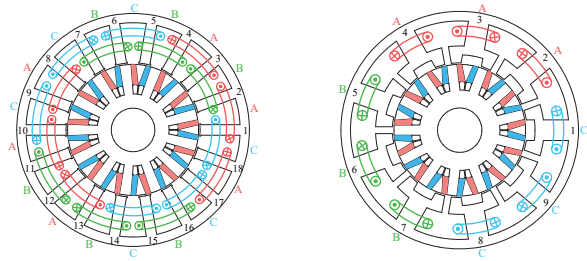

Fig. 2. Conventional PMVMs. (a) Open-slot structure (Motor 1). (b) Split-tooth structure (Motor 2).

sets, connected in star and delta connections. The hybridization of two winding sets helps mitigation of spatial harmonics in armature field and reduction of mutual coupling between both different coils of single phase and different windings of three phase. The detailed mechanism will be elaborated and analyzed in later sections.

Same as the conventional PMVMs, the investigated hybrid-CW PMVM works based on field modulation mechanism. The low-speed PM rotor magnetic field is modulated by stator teeth to interact with the high-speed armature magnetic field, realizing low-speed high-torque operation. To achieve the highest output torque capability, the relationship of stator slot number Z_s, armature pole pair p_s, and PM rotor pole pair p_r is

$$Z_s = p_s + p_r \quad (1)$$

To objectively evaluate the investigated hybrid-CW PMVM, two conventional PMVMs with open-slot (termed as Motor 1) and split-tooth (termed as Motor 2) structures [18] are selected as benchmark motors and shown in Fig. 2. As one can see, the proposed PMVM and Motor 1 employ open-slot structure with 18-stator slot, 5-armature pole pair, and 13-rotor pole pair. Motor 2 utilizes split-tooth structure with 9-stator slot, 18-auxiliary teeth, 5-armature pole pair, and 13-rotor pole pair. The key geometrical parameters of the proposed and two benchmark PMVMs are shown in Fig. 3 and listed in Table I.

The two benchmark PMVMs (i.e., Motor 1 and Motor 2) are optimized separately by the commercial finite element analysis (FEA) software JMAG 20.0, targeting high output torque, high power factor, and high PM utilization. Given that the main focus of this paper is to validate the effectiveness of the hybrid-CW on power factor improvement, the proposed PMVM adopts the same geometrical size as motor 1 because they both employ open-slot structure. This implies the proposed PMVM can be more compact since non-overlapping tooth winding is employed. Considering the ratios of phase current and turn number between delta- and star-winding sets, the proposed PMVM and motor 1 have identical electric loading, which is defined as [31]

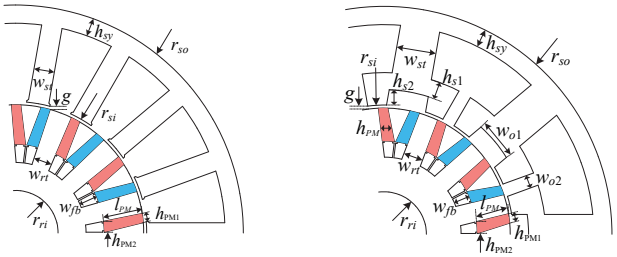

Fig. 3. Main dimensional parameters. (a) Open-slot. (b) Split-tooth.

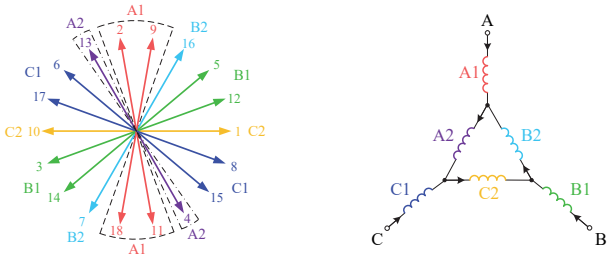

Fig. 4. Proposed hybrid-CW. (a) Star of slots. (b) Winding connection.

TABLE I
MAIN PARAMETERS OF THE INVESTIGATED PMVMS

Parameters	Proposed	Motor 1	Motor 2
Stator slot number, Z_s	18		9
Armature pole-pair number, p_s	5		
PM rotor pole-pair number, p_r	13		
Stator outer radius, r_{so} (mm)	75		
Stack length, L_{stk} (mm)	60		
Stator yoke thickness, h_{sy} (mm)	6.00		5.56
Stator teeth width, w_{st} (mm)	6.80		11.72
FMP opening width, w_{o1}/w_{o2} (mm)	/		13.04/5.60
FMP height 1, h_{s1}/ h_{s2} (mm)	/		5.63/5.04
Stator inner radius, r_{si} (mm)	43.20		42.53
Air-gap length, g (mm)	0.50		
Rotor teeth width, w_{rt} (mm)	6.40		6.61
PM thickness, h_{PM1}/ h_{PM2} (mm)	3.00/3.59		3.80/4.23
PM length, l_{PM} (mm)	13.52		11.37
Flux barrier thickness, w_{fb} (mm)	6.00		5.28
Rotor inner radius, r_{ri} (mm)	12.50		
Winding configuration	Hybrid-CW	DW	CW
Total slot area (mm^2)	5782.14		4005.40
Turns in series per phase, N_{ph}	104 (Y)/ 90 (Δ)	156	108
Current density (A/mm^2)	6		
Slot filling factor	0.42		
Rated electric loading, A_{RMS} (A/cm)	560.82		394.38
PM Volume (10^{-3} L)	69.71		67.89

$$A_{RMS} = \frac{6N_{ph}I_{RMS}}{2\pi r_{si}} \tag{2}$$

where N_{ph} is turns in series per phase, I_{RMS} is the phase current, and r_{si} is the stator inner radius. It can be seen from Table I that the optimized Motor 2 has significantly lower electric loading than Motor 1 and the proposed PMVM. The result mainly comes from two reasons, namely the reduced stator slot area and abundant MMF harmonics. The stator slot area of Motor 2 is reduced because it adopts the split-tooth structure. In addition, the electric loading of Motor 2 is designed at a low level during optimization to achieve reasonable power factor since there are abundant sub- and super-order armature MMF harmonics, as will be illustrated in later sections. Last but not least, it should be noted that the three PMVMs have nearly identical PM volume and magnetic loading.

B. Low-Harmonic Hybrid Concentrated-Winding

As shown in Fig. 1 (a), each phase of the proposed hybrid-CW comprises star- and delta-winding sets, denoted as winding 1 and 2. This winding configuration leads to mitigated mutual-coupling between different coils of single phase and that between three phase windings, as will be illustrated in the following section. With 18-slot/5-pole-pair combination, the electrical slot pitch angle of the proposed hybrid-CW is 100º and the star of slots is given in Fig. 4 (a), which represents the

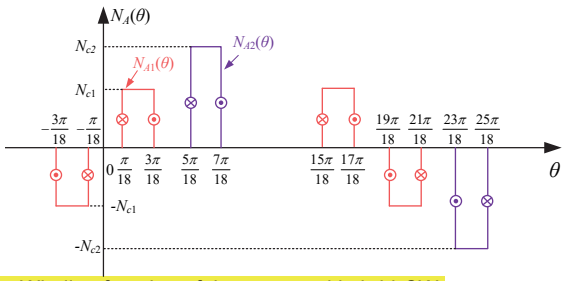

Fig. 5. Winding function of the proposed hybrid-CW.

working harmonic MMF phasor. One can see that there is a 30º electrical phase shift in space for the two winding sets. Fig. 4 (b) shows the connection of the two winding sets. From the above analysis, the proposed connection yields an amplitude ratio of $\sqrt{3}$ and a phase shift of 30º in the currents of the star and delta winding sets [32], i.e.,

$$i_1 = \sqrt{3}\cdot e^{-j\frac{\pi}{6}}\cdot i_2 \tag{3}$$

To calculate the MMF distribution of the proposed hybrid-CW, the winding function is shown in Fig. 5 and expressed as

$$N_{A1}(\theta) = \sum_{k=1,3,5...}^{\infty}(-1)^{(k-1)/2}\frac{8N_{c1}}{k\pi}\cos(k\frac{7\pi}{18})\sin(k\frac{\pi}{18})\cos[k(\theta-\frac{\pi}{2})] \tag{4}$$

$$N_{A2}(\theta) = \sum_{k=1,3,5...}^{\infty}(-1)^{(k-1)/2}\frac{4N_{c2}}{k\pi}\sin(k\frac{\pi}{18})\cos[k(\theta-\frac{\pi}{3})] \tag{5}$$

where N_{c1} and N_{c2} are the number of turns for star- and delta-winding sets. Considering the current ratio in the two winding sets as expressed in (3) and avoiding local magnetic saturation as well as fully exploiting the core material, the relationship of the turn numbers of the star- and delta-winding sets is $N_{c2} = \sqrt{3}N_{c1}$.

When symmetrical three-phase currents are supplied, the synergistic MMFs produced by the two winding sets are

$$F_{w1}(\theta,t) = \sum_{k=1,-5,7...}^{\infty}2\xi_k\cos(k\frac{7\pi}{18})\sin(k\frac{\pi}{18})\cos[k(\theta-\frac{\pi}{2})-(\omega t-\frac{\pi}{2})] \tag{6}$$

$$F_{w2}(\theta,t) = \sum_{k=1,-5,7...}^{\infty}\xi_k\sin(k\frac{\pi}{18})[k(\theta-\frac{\pi}{3})-(\omega t-\frac{\pi}{3})] \tag{7}$$

with

$$\xi_k = (-1)^{\frac{k-1}{2}}\frac{6N_{c1}I_1}{k\pi} = (-1)^{\frac{k-1}{2}}\frac{6N_{c2}I_2}{k\pi} \tag{8}$$

The synthesized three-phase armature MMF can be obtained as

$$F_t(\theta,t) = \begin{cases}\sum_{k=6n+1}^{\infty}\xi_k[2\cos(k\frac{7\pi}{18})(-1)^{\frac{k+5}{6}}+1]\sin(k\frac{\pi}{18})\cos(k\theta-\omega t)\\ \sum_{k=6n+5}^{\infty}\xi_k[2\cos(k\frac{7\pi}{18})(-1)^{\frac{k-5}{6}}+1]\sin(k\frac{\pi}{18})\cos(k\theta-\omega t)\end{cases} \tag{9}$$

Based on (9), the winding factor of the proposed hybrid-CW

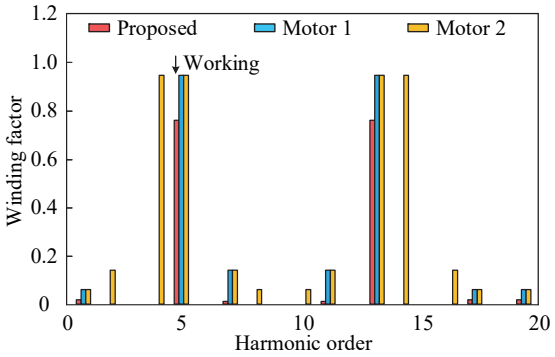

Fig. 6. Comparison of armature MMF harmonic contents.

PMVM can be obtained as shown in Fig. 6, in comparison with two benchmark PMVMs. As can be seen, except the 5th (i.e., p_sth) and 13th (i.e., p_rth) order working harmonics, there are abundant sub- and super-order MMF harmonics in Motor 2 (i.e., with conventional CW), including the 1st, 2nd, 4th, 8th, 10th, 14th and 16th harmonics. In contrast, the majority of these harmonics are reduced in Motor 1, attributed to the overlapping DW. It should be noted all these undesirable harmonics are widely cancelled in the proposed hybrid-CW PMVM. Despite the proposed hybrid-CW comprises tooth-wound coils, it exhibits a superior filtering property to both sub- and super-order MMF harmonics with the particular winding design of star-delta connection. It has been verified in [33] that the sub- and super-order MMF harmonics contribute to a significant portion of the phase inductance. Thus, the proposed low-harmonic hybrid-CW is beneficial for obtaining high power factor for the PMVMs.

III. Power Factor Improvement Mechanism

A. Power Factor of the Proposed Hybrid-CW

The hybrid-CW consists of star- and delta-winding sets and the two winding sets have different cross-section area, phase current, turn number, and coil number. Thereby, the coordinate transformations of the hybrid-CW are derived to examine the power factor.

The current and flux linkage in dq-axis frame can be obtained as

$$\begin{bmatrix} i_d \\ i_q \end{bmatrix} = \mathbf{P} \times \mathbf{P}_1 \times \begin{bmatrix} i_{a1} & i_{b1} & i_{c1} & i_{a2} & i_{b2} & i_{c2} \end{bmatrix}^{\mathrm{T}} \tag{10}$$

$$\begin{bmatrix} \varphi_d \\ \varphi_q \end{bmatrix} = \mathbf{P} \times \mathbf{P}_2 \times \begin{bmatrix} \varphi_{a1} & \varphi_{b1} & \varphi_{c1} & \varphi_{a2} & \varphi_{b2} & \varphi_{c2} \end{bmatrix}^{\mathrm{T}} \tag{11}$$

where $\mathbf{P}$ is the transformation matrix from stationary abc-axis frame to rotatory dq-axis frame, expressed as [34], [35]

$$\mathbf{P} = \frac{2}{6}\begin{bmatrix} \cos(\theta_e) & \sin(\theta_e) \\ -\sin(\theta_e) & \cos(\theta_e) \end{bmatrix} \times \begin{bmatrix} 1 & -\frac{1}{2} & -\frac{1}{2} & \frac{\sqrt{3}}{2} & -\frac{\sqrt{3}}{2} & 0 \\ 0 & \frac{\sqrt{3}}{2} & -\frac{\sqrt{3}}{2} & \frac{1}{2} & \frac{1}{2} & -1 \end{bmatrix} \tag{12}$$

where θ_e is the electrical angle of the PM rotor.

During the transformation, the space vector length of the star and delta coils should be identical. Therefore, the conversion matrix $\mathbf{P}_x$ is employed as

$$\mathbf{P}_x = \mathrm{diag}\begin{pmatrix} 1 & 1 & 1 & k_x & k_x & k_x \end{pmatrix}, x = 1,\ 2 \tag{13}$$

where x=1 and 2 refers to the conversion matrices of the current and flux linkage, respectively. Considering phase current and turn number ratios between star and delta coils, it can be found that $k_1=\sqrt{3}$ and $k_2=1/\sqrt{3}$.

The inductance in dq-axis frame is calculated as

$$\mathbf{L}_{dq} = \mathbf{P} \times \mathbf{P}_2 \times \mathbf{L}_s \times \left(\mathbf{P} \times \mathbf{P}_1\right)^{-1} \tag{14}$$

where $\mathbf{L}_s$ is the inductance matrix in stationary abc-axis frame, expressed as

$$\mathbf{L}_s = \begin{bmatrix} \mathbf{L}_{\mathrm{YY}} & \mathbf{L}_{\Delta\mathrm{Y}} \\ \mathbf{L}_{\mathrm{Y}\Delta} & \mathbf{L}_{\Delta\Delta} \end{bmatrix} \tag{15}$$

In (15), $\mathbf{L}_{\mathrm{YY}}$ and $\mathbf{L}_{\Delta\Delta}$ are the inductance matrices of the star- and delta-winding sets. $\mathbf{L}_{\mathrm{Y}\Delta}$ and $\mathbf{L}_{\Delta\mathrm{Y}}$ and the mutual inductances between star- and delta-winding sets, written as

$$\mathbf{L}_{\mathrm{YY}} = \begin{bmatrix} L_{a_1a_1} & M_{b_1a_1} & M_{c_1a_1} \\ M_{a_1b_1} & L_{b_1b_1} & M_{c_1b_1} \\ M_{a_1c_1} & M_{b_1c_1} & L_{c_1c_1} \end{bmatrix},\ \mathbf{L}_{\Delta\Delta} = \begin{bmatrix} L_{a_2a_2} & M_{b_2a_2} & M_{c_2a_2} \\ M_{a_2b_2} & L_{b_2b_2} & M_{c_2b_2} \\ M_{a_2c_2} & M_{b_2c_2} & L_{c_2c_2} \end{bmatrix} \tag{16}$$

$$\mathbf{L}_{\mathrm{Y}\Delta} = \begin{bmatrix} L_{a_2a_1} & M_{b_2a_1} & M_{c_2a_1} \\ M_{a_2b_1} & L_{b_2b_1} & M_{c_2b_1} \\ M_{a_2c_1} & M_{b_2c_1} & L_{c_2c_1} \end{bmatrix},\ \mathbf{L}_{\Delta\mathrm{Y}} = \begin{bmatrix} L_{a_2a_1} & M_{b_2a_1} & M_{c_2a_1} \\ M_{a_2b_1} & L_{b_2b_1} & M_{c_2b_1} \\ M_{a_2c_1} & M_{b_2c_1} & L_{c_2c_1} \end{bmatrix} \tag{17}$$

Substituting (12) and (13) into (11) and (14), the magnet flux linkage, q-axis inductance, and power factor of the proposed hybrid-CW are derived as

$$\varphi_{PM} = \varphi_{\mathrm{Y}} + \varphi_{\Delta}/\sqrt{3} \tag{18}$$

$$\begin{aligned} L_q &= (L_{\mathrm{Y}} + L_{\Delta}/3 + L_{\mathrm{Y}\Delta}/\sqrt{3}) - (M_{\mathrm{Y}} + M_{\Delta}/3 + M_{\mathrm{Y}\Delta}/\sqrt{3}) \\ &= L_{ph} - M_{ph} \end{aligned} \tag{19}$$

$$PF = \frac{1}{\sqrt{1+\left(L_q I_q/\varphi_{PM}\right)^2}} = \frac{1}{\sqrt{1+\left[\left(L_{ph}-M_{ph}\right)I_q/\varphi_{PM}\right]^2}} \tag{20}$$

where φ_{Y} and φ_{Δ} are the phase magnet flux linkage of the star- and delta-winding sets. $L_{\mathrm{Y}}= L_{x1x1}$, and $L_{\Delta} = L_{x2x2}$ (x= a, b, c) are the phase self-inductances of the star- and delta-winding sets, respectively. $L_{\mathrm{Y}\Delta}= L_{x1x2}$ (x= a, b, c) is the inductance between the coils that belong to one phase but different winding sets. $M_{\mathrm{Y}}= M_{x1y1}$, and $M_{\Delta} = M_{x2y2}$ (xy=ab, bc, ca) are mutual inductances of windings that belong to the same winding set but different phases. $M_{\mathrm{Y}\Delta}= M_{x1y2}$ (xy=ab, bc, ca) is the mutual inductance of windings that belong to different phases and winding sets.

Eqns. (18) and (19) indicate the magnet flux linkage and inductance of the delta-winding are converted by the turn ratio of $\sqrt{3}$. Despite the hybrid-CW configuration, the resultant various inductance components can be categorized as phase self-inductance L_{ph} and phase mutual inductance M_{ph}, of which the effects on power factor will be thoroughly analyzed in the following sections. It is worth noting that there are no physical phase self- and mutual inductances in the proposed hybrid-CW configuration. The definitions of L_{ph} and M_{ph} in Eqn. (19) are based on the coordinate transformations to conduct the inductance comparison between the proposed PMVM and the two benchmark motors.

B. Power Factor Improvement Mechanism

Each phase winding is composed of several series-connected coils. Thereby, the phase self-inductance L_{ph} comprises the coil self-inductance L_{coil_self} and coil mutual inductance L_{coil_mut} as

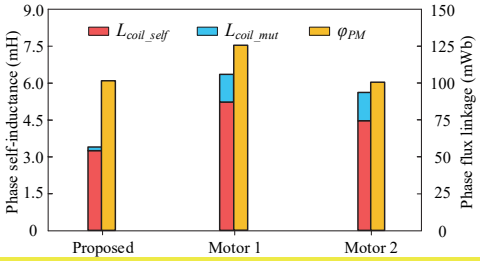

Fig. 7. Comparisons of phase self-inductance and magnet flux linkage.

TABLE II
PHASE SELF-INDUCTANCE AND ITS COMPOSITION

Items	Proposed	Motor 1	Motor 2
L_{ph} (mH)/ L^*_{ph} (10^{-1} uH/turn^2)	3.50/1.44	6.56/2.70	6.51/5.58
$L_{coil\ self}$ (mH)/ $L^*_{coil\ self}$ (10^{-1} uH/turn^2)	3.38/1.39	5.25/2.16	5.11/4.38
$L_{coil\ mut}$ (mH)/ $L^*_{coil\_mut}$(10^{-1} uH/turn^2)	0.12/0.05	1.31/0.54	1.35/1.16
ξ_{self}	0.97	0.80	0.78
φ_{PM} (mWb)	100.94	124.86	99.16
Pitch factor	0.766	0.985	0.985
Distribution factor	0.990	0.959	0.959

$$L_{ph}=\sum_{i=1}^{n_c}\frac{\varphi_{coil\_ii}}{i_{ph}}+\sum_{i\neq j}^{n_c}\frac{\varphi_{coil\_ij}}{i_{ph}}=L_{coil\_self}+L_{coil\_mut} \tag{21}$$

where i_{ph}, φ_{coil_ii}, and φ_{coil_ij} are the phase current, the armature flux linkage of the ith coil, and the mutual flux linkage among ith and jth coils. n_c is the number of coils that comprise one phase winding.

The coil self-inductance is defined as the sum of the self-inductances of coils that belong to the same phase. The coil mutual inductance is the sum of mutual inductances between different coils of one phase. Their expression can be derived as

$$\begin{aligned}L_{coil\_self}&=\sum_{i=1}^{n_c}r_gL_{stk}\int_0^{2\pi}N_{ci}(\theta)\Lambda_g(\theta)N_{ci}(\theta)d\theta\\&=\sum_{i=1}^{n_c}\sum_{h=1}^{\infty}r_gL_{stk}\frac{2N_{ph}^{\ 2}}{\pi}\left(\frac{k_{p,h}}{ht_c}\right)^2\left[2\Lambda_0+\sum_{k=1}^{\infty}\Lambda_k\cos\left(ht_c\theta_i\right)\right]\end{aligned} \tag{22}$$

$$\begin{aligned}L_{coil\_mut}&=\sum_{i=1}^{n_c}r_gL_{stk}\int_0^{2\pi}N_{ci}(\theta)\Lambda_g(\theta)N_{cj}(\theta)d\theta\\&=\sum_{i=1}^{n_c}\sum_{h=1}^{\infty}r_gL_{stk}\frac{2N_{ph}^{\ 2}}{\pi}\frac{k_{p,h}^{\ 2}}{ht_c}\times\\&\left\{2\Lambda_0\frac{\cos\left[ht_c\left(\theta_i-\theta_j\right)\right]}{ht_c}+\sum_{k=1}^{\infty}\Lambda_k\frac{\cos\left[ht_c\theta_i+\left(kZ_s\pm ht_c\right)\theta_j\right]}{\left(kZ_s\pm ht_c\right)}\right\}\end{aligned} \tag{23}$$

where r_g is the air-gap radius. L_{stk}, $k_{p,h}$ and θ_i are stack length, the pitch factor of the hth-order armature field harmonic, and space angle of the ith coil. N_{ci} and N_{cj} are the winding function of the ith and jth coils. Λ_g is the air-gap permeance, with Λ_0 and Λ_k the fundamental and kth-order components.

The phase magnet flux linkage is expressed as

$$\begin{aligned}\varphi_{PM}(\theta,t)=&\sum_{i=1,3,5\ldots}2F_{ei}r_gL_{stk}N_{ph}\times\\&\left(\sum_{ht_c=ip_r}\Lambda_0\frac{k_{p,h}k_{d,h}}{ht_c}+\sum_{ht_c=|ip_r\pm kZ_s|}\frac{\Lambda_k}{2}\frac{k_{p,h}k_{d,h}}{ht_c}\right)\cos\left(ip_r\omega_rt\right)\end{aligned} \tag{24}$$

where F_{ei} is the ith-order PM MMF harmonic, and $k_{d,h}$ is the distribution factor of the hth-order armature field harmonic.

From (22) to (24), it can be seen that both the coil self- and mutual inductances are proportional to square of the pitch factor, while the magnet flux linkage is in proportion to the pitch factor. Therefore, the power factor can be improved by adopting proper short-pitch winding, since the reduction of inductances is more significant than that of magnet flux linkage. In addition, (23) indicates that the coil mutual inductance is in close relation to the spatial distribution between different coils of one phase. Different space distributions of coils can affect the magnet flux linkage through distribution factor. Therefore, the coils comprising one phase should be arranged in such a way that the distribution factor is maintained while the mutual inductances among the coils are reduced. As a result, the coil mutual inductances can be reduced to improve the power factor, without impairing the output torque capability.

The comparisons of the phase self-inductance components and phase magnet flux linkage are presented in Fig. 7 and listed in Table II. The inductances are calculated by 3D FEA with frozen permeability method to take local saturation and end-leakage inductance into consideration. To account for different winding turn numbers of the three investigated PMVMs, the scaled inductance per turn (i.e., labeled with "*") is defined as the ratio of inductance to the square of turn number in series per phase. The scaled phase self-inductance and its compositions are listed in Table II.

From Table II, since Motor 1 and the proposed PMVM have low-harmonic MMF contents, their scaled coil self-inductances $L^*_{coil\ self}$ are proportional to the square of the pitch factor, while their magnet flux linkages are proportional to pitch factor. This validates the aforementioned analysis that the power factor can be improved by adopting proper short-pitch winding. In particular, the proposed PMVM exhibits 19.16% lower magnet flux linkage but 35.62% lower coil self-inductance, when compared with Motor 1. In addition, by proper arrangement of coils that belong to one phase, the coil mutual inductance of the proposed PMVM L_{coil_mut} is reduced by 90.84% whereas the distribution factor is even higher than Motor 1. This contributes to further power factor improvement without impairing output torque capability. Meanwhile, Motor 2 exhibits the largest scaled coil self- and mutual inductances (i.e., $L^*_{coil\ self}$ and $L^*_{coil\ mut}$) due to abundant sub- and super-order MMF harmonics. With higher winding turn number and electric loading, the proposed PMVM even exhibits 33.86% lower coil self-inductance and 91.11% lower coil mutual inductance than Motor 2. In table II, ξ_{self} is defined as the ratio of coil self-inductance L_{coil_self} to phase self-inductance L_{ph}. The above analysis implies higher ξ_{self} can achieve a higher power factor. As one can see, the proposed hybrid-CW exhibits the highest ξ_{self} and the lowest coupling between different coils of one phase, which is the first fold essence of the low-coupling design.

The three-phase windings can be perceived as three virtual composite coils, with both 120º electrical phase shift in space and time. Thus, the distribution factor of the three phases is always unity. From the foregoing analysis, the mutual inductances between three phases can be reduced by proper winding configuration to improve the power factor with no reduction on magnet flux linkage and output torque production capability. This is in accordance with the common perception of negligible reluctance torque in PMVMs.

To examine the mutual phase coupling, the field distributions of the three motors with only one phase excitation (i.e., phase A) are shown in Fig. 8. It can be seen that noticeable mutual phase coupling is observed in Motor 1, attributed to the adopted

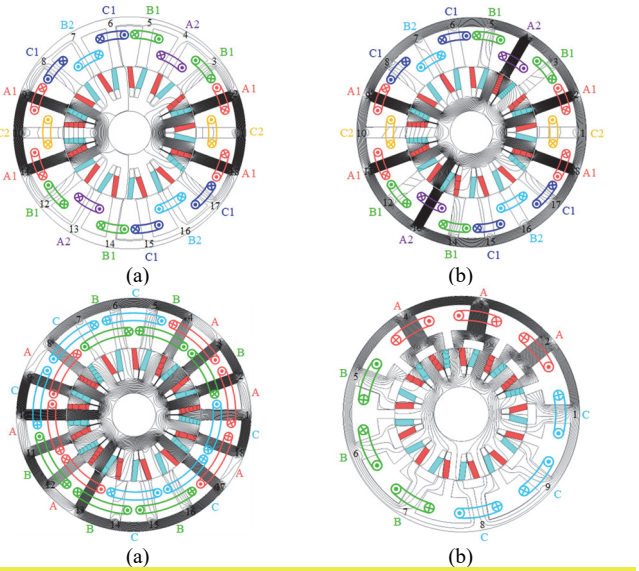

Fig. 8. Field distributions when only phase A is excited. (a) Proposed PMVM (rotor position 1). (b) Proposed PMVM (rotor position 2). (c) Motor 1. (d) Motor 2.

TABLE III
COMPARISON OF INDUCTANCES AND POWER FACTOR

Items	Proposed	Motor 1	Motor 2
Phase self-inductance, L_{ph} (mH)	3.50	6.56	6.51
Phase mutual inductance, M_{ph} (mH)	0.09	1.15	0.42
q-axis inductance, L_q (mH)	3.59	7.71	6.93
L_q/φ_{PM} (mH/Wb)	35.57	61.75	69.89
Power factor	0.96	0.83	0.75

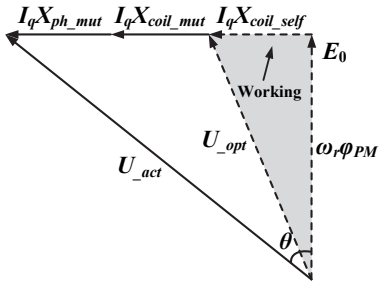

Fig. 9. Phasor diagram of the PMVM with I_d=0 control.

overlapping DW, while Motor 2 presents significantly reduced mutual phase coupling by adopting the conventional CW. In the proposed hybrid-CW PMVM, the mutual phase coupling is almost eliminated. As verified in Table III, through the low-coupling hybrid-CW, the phase mutual inductance of the proposed PMVM can be reduced by 92.17% and 78.57% as compared with the two conventional PMVMs. These gained results comply with the armature MMF distribution in Fig. 5.

In summary, there are mainly two inductance components in PMVMs, namely phase self- and phase mutual inductances. The phase self-inductance can be further divided as coil self- and coil mutual inductances, as depicted in Fig. 9. Through the proper selection of short coil pitch, the coil self-inductance L_{coil_self} is reduced more significantly than the magnet flux linkage φ_{PM}, leading to an improved power factor. As demonstrated in Fig. 9, the terminal voltage can be reduced from actual voltage $U_{\_act}$ to the optimal voltage $U_{\_opt}$ by eliminating the coil mutual inductance L_{coil_mut} and phase mutual inductance M_{ph}. Meanwhile, the magnet flux linkage

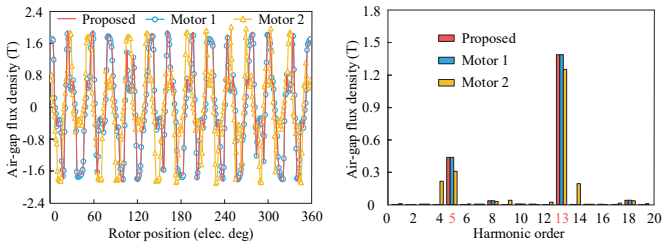

Fig. 10. Open-circuit air-gap flux densities. (a) Waveform. (b) Spectrum.

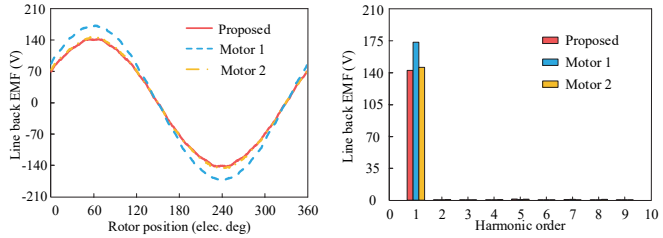

Fig. 11. No-load back-EMFs at 600 r/min. (a) Waveform. (b) Spectrum.

φ_{PM} is maintained. Therefore, the power factor can be further improved by eliminating the mutual coupling between coils of each phase and those between three phase windings.

Based on foregoing analysis, the proposed hybrid-CW is an effective solution to improve power factor for PMVM, through proper coil pitch selection and low-coupling winding design. In particular, the low-coupling design has twofold essences, namely the coupling between different coils of single phase and that between different windings of three phase are suppressed significantly. As compared with Motor 1 and Motor 2, the proposed PMVM exhibits 46.65% and 46.24% lower phase self-inductance, as well as 92.17% and 78.57% lower phase mutual inductance. The ratio of q-axis inductance to PM flux linkage is reduced significantly, and the proposed PMVM can achieve power factor as high as 0.96, as compared with 0.83 and 0.75 from Motor 1 and Motor 2, respectively.

IV. PERFORMANCE COMPARISON

To objectively evaluate the electromagnetic performances of the proposed hybrid-CW PMVM, a comprehensive comparison is conducted with the two conventional PMVMs, in terms of no-load back electromotive force (EMF), torque density, power factor and efficiency. The main design parameters of the three motors are listed in Table I.

A. No-Load Field Distribution and Back-EMF

The no-load air-gap flux densities of the three motors are compared in Fig. 10. For the proposed PMVM and Motor 1 employing open-slot stator structure, there are mainly two working harmonics, namely p_sth (i.e., 5th) and p_rth (i.e., 13th) order harmonics. Meanwhile, there are additional harmonics emerging in Motor 2 employing split-tooth structure, among which the 4th-order sub-harmonic can contribute to back-EMF and torque production at the sacrifice of power factor [36].

The line back-EMF comparison is shown in Fig. 11. With the same slot area and identical open-circuit airgap flux density distribution, the proposed PMVM has 17.85% lower back-EMF than Motor 1, owing to the shorter coil pitch and lower pitch

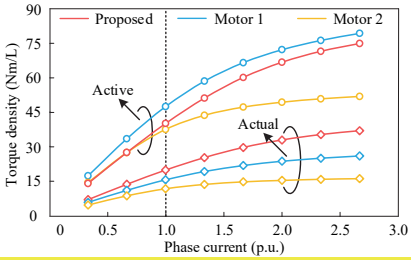

Fig. 12. Torque density comparisons (with rated phase current amplitude of 23 A).

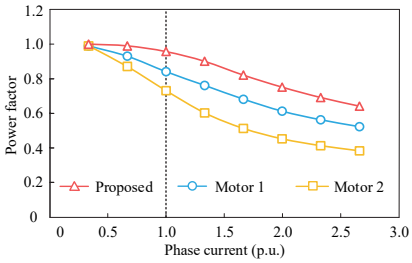

Fig. 13. Power factor comparisons (with rated phase current amplitude of 23 A).

factor. Meanwhile, the proposed PMVM exhibits comparable back-EMF with Motor 2, though Motor 2 consists of a reduced slot area caused by the split-tooth structure. This feature is mainly due to the higher pitch factor of Motor 2, and the newly generated 4th-order sub-harmonic has a lower pole pair and higher back-EMF production capability.

B. Electromagnetic Torque and Power Factor

To account for the end-winding volume, the end-winding length is calculated by assuming a semicircular shape as [32]

$$l_{ew} = \pi \cdot (r_{ew} + \frac{w_{st}}{2}), \quad r_{ew} = \pi \frac{r_w}{Z_s} \times K_s \tag{25}$$

where r_w is the average radius of the stator winding, K_s is the coil pitch, and w_{st} is the stator tooth width.

With i_d=0 control and rated current density of 6 A/mm^2, the output torque capabilities of the three PMVMs are compared in Fig. 12 and listed in Table IV. The three investigated PMVMs have identical phase current amplitude of 23 A. As illustrated in Table I, the proposed PMVM and Motor 1 have identical electric loading of 560.82 A/cm, while Motor 2 has a relatively low electric loading of 394.38 A/cm due to the abundant sub- and super-order MMF harmonics. It can be seen at the rated condition, the proposed PMVM exhibits an active torque density of 39.99 Nm/L, and an actual torque density (i.e., with end-winding volume taken into account) of 21.98 Nm/L. In addition, Motor 1 has the largest active torque density while Motor 2 is subject to the lowest output torque due to the reduced slot area and severe trade-off between output torque and power factor. With end-winding volume considered, the proposed PMVM exhibits the highest actual torque density. In particular, at the rated condition, the proposed PMVM has 22.52% and 52.43% higher actual torque density than Motor 1 and Motor 2, respectively. Furthermore, under heavy load conditions, the proposed hybrid-CW PMVM has comparable output torque as Motor 1, due to lower magnetic saturation.

Fig. 13 presents the power factor comparisons of the three PMVMs at different load conditions. It shows that the proposed

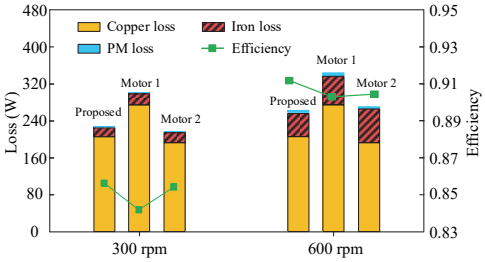

Fig. 14. Loss and efficiency comparisons under different speeds.

TABLE IV
ELECTROMAGNETIC PERFORMANCE COMPARISONS AT RATED CONDITION

Parameters	Proposed	Motor 1	Motor 2
Average torque (Nm)	42.40	50.20	39.65
Active torque density (Nm/L)	39.99	47.34	37.40
Actual stack length (mm)	109.16	158.34	155.6
Actual torque density (Nm/L)	21.98	17.94	14.42
Copper losses (W)	204.67	273.12	191.63
Core losses (W)	53.68	66.53	75.01
Efficiency	91.16%	90.28%	90.33%

PMVM exhibits a significant power factor improvement over the two benchmark PMVMs. In particular, the power factor of the proposed PMVM can be improved to 0.96 from 0.83 (Motor 1) and 0.75 (Motor 2), with rated electric loading given in Table I. The power factor improvement is achieved by proper coil pitch selection and low-coupling design. The employment of short coil pitch contributes to reducing phase self-inductance remarkably. Furthermore, low-coupling design has twofold essences, i.e., both the mutual coupling between different coils of single phase and that between different windings of three phases suppressed substantially.

C. Losses and Efficiency

The loss and efficiency comparisons of the three motors are shown in Fig. 14, with a rated speed of 600 rpm. As one can see, the copper loss is dominant at low-speed direct drive operation. Although the proposed PMVM and Motor 1 have identical slot area, the proposed PMVM features a much lower copper loss than motor 1, attributed to the reduced end-winding length. In addition, Motor 2 exhibits comparable copper loss with the proposed PMVM, despite the larger end-winding length. This is because Motor 2 has reduced slot area due to the adopted split-tooth structure.

Operating at 300 r/min, the proposed PMVM exhibits the highest efficiency of 85.58%, due to the lower copper loss than Motor 1 and larger output torque than Motor 2. As listed in Table IV, at the rated speed of 600 r/min, the efficiency of the proposed PMVM can be improved to 91.16%, as compared with 90.28% (Motor 1) and 90.33% (Motor 2). The efficiency improvement is owing to the reduced iron losses as the proposed hybrid-CW has a good filtering property to both sub- and super-order harmonics.

V. EXPERIMENTAL VALIDATION

The proposed hybrid-CW PMVM is fabricated to validate the forgoing analysis and the FEA results, with the main design parameters listed in Table I. Fig. 15 shows the prototype and on-load test bench. As shown in Fig. 15 (a), the iron bridge is adopted in the rotor structure to connect the separate iron poles and enhance the mechanical strength. The control system

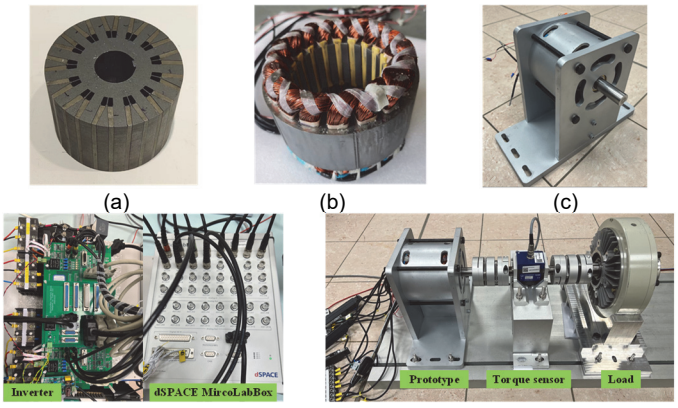

Fig. 15. Prototype and test rig. (a) Rotor. (b) Stator. (c) The proposed PMVM prototype. (d) Control system. (e) Test rig.

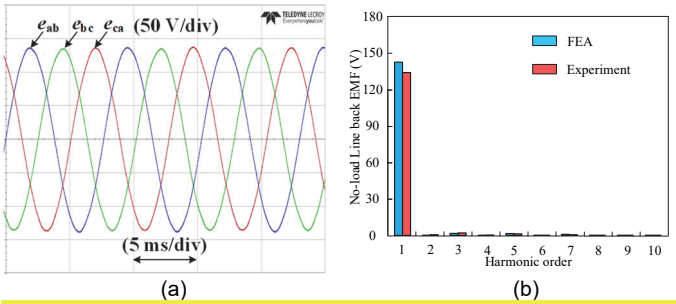

Fig. 16. No-load line back EMF at 600r/min. (a) Experimental waveform. (b) Harmonic spectrums compared with FEA results.

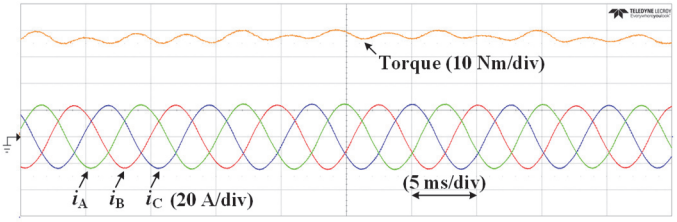

Fig. 17. Measured steady-state torque and current waveforms when operating at 600 r/min with the rated phase current of 23 A (amplitude).

consists of a three-phase voltage source inverter and dSPACE MicroLabBox. The PMVM prototype is connected to the load (i.e., magnetic braking) through a HBM torque transducer T21WN. The electric and torque signals are displayed in a high-performance oscilloscope LECROY-MDA 8058HD.

Fig. 16 (a) shows the measured open-circuit line back-EMF waveforms when the PMVM prototype is driven by a servo motor at rated 600 r/min. It can be found that the three-phase back-EMFs are symmetrical and sinusoidally distributed, exhibiting a low total harmonic distortion (THD) of 2.24%. Meanwhile, the harmonic spectrums of the measured and FEA-predicted back-EMFs are compared in Fig. 16 (b). A good consistency is observed in the FEA and experimental results, with a 5.9% discrepancy in the fundamental component. The error is acceptable and mainly caused by the end effect as well as manufacturing imperfection.

In addition, the on-load test is conducted with i_d=0 control and a rated phase current amplitude of 23 A. When the PMVM prototype is operated at the rated speed of 600 r/min, the measured output torque and three-phase current waveforms are shown in Fig. 17. The measured average torque is 38.13 Nm,

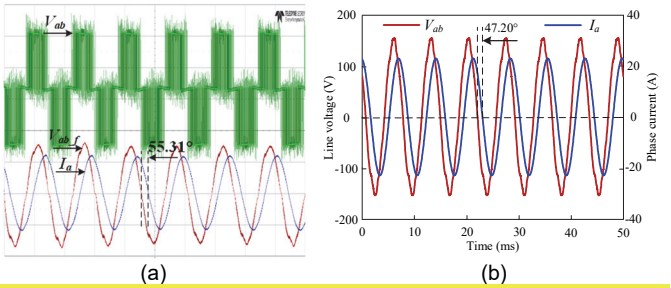

Fig. 18. Power factor validation at rated condition. (a) Experimental waveform (5 ms/div, 100 V/div, 20 A/div). (b) Simulation results.

TABLE V
MEASURED ELECTROMAGNETIC PERFORMANCES AT RATED CONDITION

	Torque (Nm)	L_Y (mH)	L_Δ (mH)	*PF*	η (%)	Error (torque)
FEA	42.40	2.26	3.47	0.96	91.16	\
Experiment	38.13	2.08	3.50	0.90	89.27	10.07%

which is 10.07% lower than the simulated result. The error is mainly attributed to the friction force and property discrepancy of steel materials used in simulation and experiments. In particular, the measured friction torque is around 0.6 Nm, and the magnetic permeability of the prototype steel material is affected by the adopted wire cut fabrication technology, making the prototype suffer from more severe magnetic saturation.

As it is difficult to measure mutual inductances, the self-inductances of star- and delta-winding sets (i.e., L_Y and L_Δ) are measured and the results are compared with that obtained by 3D FEA, as listed in Table V. The simulated and measured inductances demonstrate good agreement, with a discrepancy less than 8%. Furthermore, the power factor validation is conducted by measuring the phase angle between line voltage V_{ab} and line current I_{ab}. For simplicity, the line voltage V_{ab} and phase current I_a are measured as shown in Fig. 18, where V_{ab} is the line voltage generated by the voltage source inverter (VSI) and V_{ab_f} is the fundamental component of V_{ab}, obtained by filtering out the high-frequency switching harmonics by the built-in Finite Impulse Response (FIR) filter of the oscilloscope [37]. It should be mentioned that the FIR filter has a linear response and the phase delay caused by filtering is compensated by the built-in function of the oscilloscope. Furthermore, for symmetrical three phase system, I_{ab} is 30° phase leading than I_a. Therefore, the simulated and measured phase angles between line voltage V_{ab} and line current I_{ab} are 17.20°and 25.31°. It can be calculated that the simulated and measured power factors are 0.955 and 0.904. The experimental error in measured power factor is mainly attributed to the drop in the measured output torque. Specifically, the reduction of measured output torque reflects magnet flux linkage discrepancy of about 10% since i_d=0 control is utilized. Nevertheless, the measured inductance agrees well with the simulated results. As a result, the practical ratio of inductance to magnet flux linkage is increased due to manufacturing discrepancy, which tends to deteriorate the power factor. In addition, the measurement error in the phase angles of line voltage and current could result in a reduction of the measured power factor.

The rated performance metrics obtained from experiments and simulation are listed in Table V. Although the measured

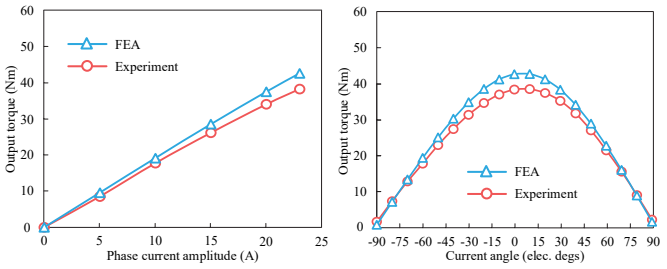

(a) (b)

Fig. 19. Output torque comparisons. (a) Torque versus phase current amplitude. (b) Torque versus current angle.

power factor (i.e., 0.90) is slightly lower than the predicted result (i.e., 0.96), the investigated hybrid-CW PMVM is an effective solution to improve power factor for PMVMs. The measured and calculated phase resistances of the star- and delta-winding sets are 0.18 Ω *vs*. 0.17 Ω and 0.26 Ω *vs*. 0.26 Ω, respectively. It is found that the measured and calculated copper losses are 206.1 W and 197.9 W, exhibiting good agreement. Meanwhile, there is a minor discrepancy in the experimental and simulated efficiencies. The error is mainly due to the reduced output torque and friction losses (around 37.7 W). Although the hybrid-CW introduces circulating current in the delta-winding set, the measured circulating current is 1.69 A (rms), resulting in negligible extra copper losses of 2.2 W.

Furthermore, the output torque versus current amplitude waveform is shown in Fig. 19 (a). As can be seen, the discrepancy between simulation and measured results increases along with the current amplitude, attributed to the more severe saturation level and flux leakage. With a rated phase current of 16 A (rms), the output torque versus current angle curve is depicted in Fig. 19 (b). It can be seen that the measured and simulated results exhibit the same variation trend and a good agreement. The optimal current angle is around 0°, indicating the reluctance torque is negligible in the proposed PMVM and i_d=0 control should be employed.

VI. Conclusion

This paper presents a new winding concept, i.e., low-coupling hybrid-CW to improve the power factor of PMVMs. Analysis shows that the proposed hybrid-CW has a good filtering property to both sub- and super-order harmonics, which is advantageous for obtaining high power factor. The power factor of the investigated PMVM is significantly improved by the low-coupling hybrid-CW, through the meticulous selection of short coil pitch and low-coupling design. Some findings are obtained as:

1) For PMVMs subject to low power factor, the designs with short-pitch winding and low pitch factor may provide superior performance over full-pitch winding, in terms of power factor and actual torque density.

2) The phase self-inductance consists of coil self- and coil mutual inductances. By meticulous design of short coil pitch, a lower ratio of coil self-inductance to PM flux linkage can be achieved, leading to enhanced power factor.

3) The coil mutual inductances between different coils of single phase can be reduced through proper coil arrangement to further improve the power factor.

4) The phase mutual inductances can be eliminated to further enhance the power factor without impairing output torque.

Experimental results validate that the proposed PMVM with low-coupling hybrid-CW exhibits an active torque density around 40 Nm/L and a high power factor up to 0.96, exhibiting great improvement than conventional designs and excellent prospect in direct-drive applications.

References

[1] X. Zhao and S. Niu, "A new slot-PM vernier reluctance machine with enhanced zero-sequence current excitation for electric vehicle propulsion," *IEEE Trans. Ind. Electron*., vol. 67, no. 5, pp. 3528–3539, May. 2020.

[2] C. Liu, K. T. Chau, C. H. T. Lee and Z. Song, "A critical review of advanced electric machines and control strategies for electric vehicles," *Proc. IEEE*, vol. 109, no. 6, pp. 1004-1028, Jun. 2021.

[3] J. Yu and C. Liu, "Design of a double-stator magnetless vernier machine for direct-drive robotics," *IEEE Trans. Magn.*, vol. 54, no. 11, Nov. 2018.

[4] C. Gong and F. Deng, "Design and optimization of a high-torque-density low-torque-ripple vernier machine using ferrite magnets for direct-drive applications," *IEEE Trans. Ind. Electron.*, vol. 69, no. 6, pp. 5421–5431, Jun. 2022.

[5] H. Chen, Y. Zuo, K. T. Chau, W. Zhao, and C. H. T. Lee, "Modern electric machines and drives for wind power generation: A review of opportunities and challenges," *IET Renewable Power Generation,* vol.15*,* no.9, Feb. 2021.

[6] M. Cheng, P. Han, and W. Hua, "A general airgap field modulation theory for electrical machines," *IEEE Trans. Ind. Electron.*, vol. 64, no. 8, pp. 6063–6074, Aug. 2017.

[7] X. Zhu, C. H. T. Lee, C. C. Chan, L. Xu, and W. Zhao, "Overview of flux-modulation machines based on flux-modulation principle: Topology, theory and development prospects," *IEEE Trans. Transp. Electrific.*, vol. 6, no. 2, pp. 612–624, Jun. 2020.

[8] Z. Q. Zhu and Y. Liu, "Analysis of air-gap field modulation and magnetic gearing effect in fractional slot concentrated winding permanent magnet synchronous machines," *IEEE Trans. Ind. Electron*., vol. 65, no. 5, pp. 3688–3698, May. 2018.

[9] S. Xie, H. Chen, Y. Zuo, F. Shen, B. S. Han, C. C. Hoang, and C. H. T. Lee, "A consequent-pole magnetic-geared machine with axially embedded permanent magnets for hybrid electric vehicle," *IEEE Access*, vol. 9, pp. 14905–14917, Jan. 2021.

[10] N. J. Baker, M. A. H. Raihan, A. A. Almoraya, J. W. Burchell, and M. A. Mueller, "Evaluating alternative linear vernier hybrid machine topologies for integration into wave energy converters," *IEEE Trans. Energy Convers.*, vol. 33, no. 4, pp. 2007–2017, Dec. 2018.

[11] B. Kim and T. A. Lipo, "Analysis of a PM vernier motor with spoke structure," *IEEE Trans. Ind. Appl.*, vol. 52, no. 1, pp. 217–225, Jan. 2016.

[12] Y. Zhao, D. Li, M. Lin and R. Qu, "Investigation of line-start permanent magnet vernier machine with different rotor topologies," *IEEE J. Emerg. Sel. Topics Power Electron*., Early Access, doi: 10.1109/JESTPE. 2021.3061120.

[13] W. Liu, J. Wang and T. A. Lipo, "A consequent pole single rotor single stator vernier design to effectively improve torque density of an industrial PM drive," *IEEE Trans. Ind. Electron*., Early Access, doi: 10.1109/TIE.2022.3153806.

[14] X. Ren, D. Li, R. Qu, Z. Yu, and Y. Gao, "Investigation of spoke array permanent magnet vernier machine with alternate flux bridges," *IEEE Trans. Energy Conv.*, vol. 33, no. 4, pp. 2112–2121, Dec. 2018.

[15] D. Li, R. Qu, and T. A. Lipo, "High-power-factor vernier permanent magnet machines," *IEEE Trans. Ind. Appl*., vol. 50, no. 6, pp. 3664–3674, Nov. 2014.

[16] F. Zhao, T. A. Lipo, and B.-I. Kwon, "A novel dual-stator axial-flux spoke-type permanent magnet vernier machine for direct-drive applications," *IEEE Trans. Magn.*, vol. 50, no. 11, Nov. 2014.

[17] S. Xie, Y. Zuo, H. Chen, L. Cao, X. Yuan, B. Han, C. Hoang and C. H. T. Lee, "Investigation on stator shifting technique for permanent magnet vernier machines with two-slot pitch winding," *IEEE Trans. Ind. Electron.*, Early Access, doi: 10.1109/TIE.2022. 3201308.

[18] Y. Liu, H. Li, and Z. Zhu, "A high-power factor vernier machine with coil pitch of two slot pitches," *IEEE Trans. Magn.*, vol. 54, no. 11, pp. 1-5, May. 2018.

[19] T. Zou, D. Li, R.Qu, J. Li, and D. Jiang, "Analysis of a dual-rotor, toroidal winding, axial-flux vernier permanent magnet machine," *IEEE Trans. Ind. Appl.*, vol. 53, no. 3, pp. 1920–1930, May. 2017.
[20] D. Li, T. Zou, R. Qu, and D. Jiang, "Analysis of fractional-slot concentrated winding PM vernier machines with regular open-slot stators," *IEEE Trans. Ind. Appl.*, vol. 54, no. 2, pp. 1320–1330, Mar. 2018.
[21] L. Xu *et al.*, "Quantitative comparison of integral and fractional slot permanent magnet vernier motors," *IEEE Trans. Energy Convers.*, vol. 30, no. 4, pp. 1483–1495, Dec. 2015.
[22] S. M. Raziee, O. Misir, and B. Ponick, "Combined star-delta winding analysis," *IEEE Trans. Energy Convers*., vol. 33, no. 1, pp. 383–394, Mar. 2018.
[23] W. Zhao, J. Zheng, J. Ji, S. Zhu, andM. Kang, "Star and delta hybrid connection of fraction-slot concentrated-winding PM machine for low space harmonics," *IEEE Trans. Ind. Electron.*, vol. 65, no. 12, pp. 9266–9279, Dec. 2018.
[24] Y. Lei, Z. Zhao, S. Wang, D. G. Dorrell and W. Xu, "Design and analysis of star–delta hybrid windings for high-voltage induction motors," *IEEE Trans. Ind. Electron*., vol. 58, no. 9, pp. 3758-3767, Sept. 2011.
[25] H. Vansompel, P. Sergeant, L. Dupre, and A. Van den Bossche, "A combined wye-delta connection to increase the performance of axial-flux PM machines with concentrated windings," *IEEE Trans. Energy Convers.*, vol. 27, no. 2, pp. 403–410, Jun. 2012.
[26] M. N. Ibrahim, P. Sergeant and E. M. Rashad, "Combined star-delta windings to improve synchronous reluctance motor performance" *IEEE, Trans. Energy Convers*., vol. 31, no. 4, pp. 1479-1487, Dec. 2016.
[27] A. S. Abdel-Khalik, S. Ahmed, and A. M. Massoud, "Effect of multilayer windings with different stator winding connections on interior PM machines for EV applications," *IEEE Trans. Magn.*, vol. 52, no. 2, pp. 1–7, Feb. 2016.
[28] S. Sadeghi, L. Guo, H. A. Toliyat, and L. Parsa, "Wide operational speed range of five-phase permanent magnet machines by using different stator winding configurations," *IEEE Trans. Ind. Electron.*, vol. 59, no. 6, pp. 2621–2631, 2012.
[29] A. S. Abdel-Khalik, M. A. Elgenedy, S. Ahmed, and A. M. Massoud, "An improved fault-tolerant five-phase induction machine using a combined star/pentagon single layer stator winding connection," *IEEE Trans. Ind. Electron*., vol. 63, no. 1, pp. 618–628, Jan. 2016.
[30] B. Wang, L. Luo, W. Hua, M. Cheng and S. Niu, "High performance and strong fault tolerant triple 3-phase PMa-SynRM with star-delta windings," *IEEE Trans. Energy Convers*., vol. 37, no. 3, pp. 1977-1986, Sept. 2022.
[31] T. A. Lipo, Introduction to AC Machine Design. Madison, WI, USA: Univ. Wisconsin, 2011, pp. 335–371.
[32] G. Dajaku, H. Hofmann, F. Hetemi, X. Dajaku, W. Xie, and D. Gerling, "Comparison of two different IPM traction machines with concentrated winding," *IEEE Trans. Ind. Electron.*, vol. 63, no. 7, pp. 4137–4149, Jul. 2016.
[33] R. Dutta, L. Chong, and M. F. Rahman, "Winding inductances of an interior permanent magnet (IPM) machine with fractional slot concentrated winding," *IEEE Trans. Magn.*, vol. 48, no. 12, pp. 4842–4849, Dec. 2012.
[34] P. C. Krause, O. Wasynczuk, and S. D. Sudhoff, *Analysis of Electric Machinery and Drive Systems*, 2nd ed. Hoboken, NJ, USA: Wiley, 2002.
[35] M. N. Ibrahim, P. Sergeant, and E. E. M. Rashad, "Combined star-delta windings to improve synchronous reluctance motor performance," *IEEE Trans. Energy Convers.*, vol. 31, no. 4, pp. 1479–1487, Dec. 2016.
[36] T. Zou, D. Li, C. Chen, R. Qu, and D. Jiang, "A multiple working harmonic PM vernier machine with enhanced flux-modulation effect," *IEEE Trans. Magn.*, vol. 54, no. 11, Nov. 2018.
[37] Application note an-006 digital oscilloscopes enhanced resolution. Accessed: 2021-10-20. [Online]. Available: https://teledynelecroy.com/doc/digital- oscilloscopes-enhanced-resolution.

Shuangchun Xie (S'20) received his B.Sc. degree in electrical engineering and automation from Nanjing University of Aeronautics and Astronautics, Nanjing, China, in 2017. He is currently working toward the Ph.D. degree in School of Electrical and Electronic Engineering, Nanyang Technological University, Singapore.

Shun Cai received the B.Eng. and M.Sc. degrees from Zhejiang University, Hangzhou, China, in 2014 and 2017, respectively and the Ph.D. degree from the University of Sheffield, Sheffield, U.K., in 2020. Since 2021, He has been a Research Fellow with Nanyang Technological University, Singapore.

Yuefei Zuo (M'18) received the B.Sc. and the Ph. D. degrees in electrical engineering and automation from Nanjing University of Aeronautics and Astronautics, Nanjing, China, in 2010 and 2016, respectively. He is currently a Postdoctoral Research Fellow with Nanyang Technological University, Singapore.

Libing Cao (S'17-M'22) received the B.Eng. degree in electrical and electronic engineering from Zhejiang University, Hangzhou, China, in 2016, and the Ph.D. degree in electrical and electronic engineering from The University of Hong Kong, Pokfulam, Hong Kong, in 2020. He is currently a Postdoctoral Research Fellow with Nanyang Technological University, Singapore.

Jingwei Zhu received the B.Sc. degree in electrical engineering and automation from Zhejiang University, Hangzhou, China, in 2015, and the M.Phil. degree in electrical engineering from The Hong Kong Polytechnic University, Hong Kong, in 2018. Since August 2020, he has been working toward the Ph.D. degree in Nanyang Technological University, Singapore.

An Li (S'17) received his B.Eng. degree and Ph.D. degree both in electrical engineering from School of Electrical and Electronic Engineering, Huazhong University of Science and Technology, Wuhan, China, in 2017 and 2022, respectively. His research interests include motor drives, power electronic converter, reluctance machine and multiphase machine.

Yuming Yan received the B.Sc. degree in electrical engineering from Xi'an Jiaotong University (XJTU), Xi'an, China in 2017. He is currently working toward the Ph.D. degree in School of Electrical and Electronic Engineering, Nanyang Technological University, Singapore.

His research interests include electric machines and drives, fault tolerant machines, and renewable energy generation.

Christopher H. T. Lee (M'12-SM'18) received his B.Eng. (First Class Honours) degree, and Ph.D. degree both in electrical engineering from Department of Electrical and Electronic Engineering, The University of Hong Kong, Hong Kong, in 2009 and 2016, respectively.

He currently serves as an Assistant Professor at Nanyang Technological University, Singapore and Honorary Assistant Professor at The University of Hong Kong, Hong Kong. He was a Postdoctoral Fellow and then a Visiting Assistant Professor at Massachusetts Institute of Technology, United States. He is an Associate Editor for IEEE Transactions on Industrial Electronics, IEEE Transactions on Energy Conversion, IEEE Access and IET Renewable Power Generation. His research interests include Electric Machines and Drives, Renewable Energies, and Electromechanical Propulsion Technologies. In these areas, he has published 1 book, 3 books chapters, and over 140 referred papers.